

The following resources related to this article are available online at www.sciencemag.org (this information is current as of July 30, 2009):

Updated information and services, including high-resolution figures, can be found in the online version of this article at:

<http://www.sciencemag.org/cgi/content/full/317/5839/780>

Supporting Online Material can be found at:

<http://www.sciencemag.org/cgi/content/full/317/5839/780/DC1>

A list of selected additional articles on the Science Web sites **related to this article** can be found at:

<http://www.sciencemag.org/cgi/content/full/317/5839/780#related-content>

This article **cites 21 articles**, 4 of which can be accessed for free:

<http://www.sciencemag.org/cgi/content/full/317/5839/780#otherarticles>

This article has been **cited by** 27 article(s) on the ISI Web of Science.

This article appears in the following **subject collections**:

Physics, Applied

http://www.sciencemag.org/cgi/collection/app_physics

Information about obtaining **reprints** of this article or about obtaining **permission to reproduce this article** in whole or in part can be found at:

<http://www.sciencemag.org/about/permissions.dtl>

Multifunctional Nanomechanical Systems via Tunably Coupled Piezoelectric Actuation

Sotiris C. Masmanidis,¹ Rassul B. Karabalin,¹ Iwijn De Vlaminck,² Gustaaf Borghs,² Mark R. Freeman,³ Michael L. Roukes^{1*}

Efficient actuation is crucial to obtaining optimal performance from nanoelectromechanical systems (NEMS). We employed epitaxial piezoelectric semiconductors to obtain efficient and fully integrated NEMS actuation, which is based on exploitation of the interaction between piezoelectric strain and built-in charge depletion. The underlying actuation mechanism in these depletion-mediated NEMS becomes important only for devices with dimensions approaching semiconductor depletion lengths. The induced actuation forces are controlled electrically, and resonant excitation approaching single-electron efficiency is demonstrated. The fundamental electromechanical coupling itself can be programmed by heterostructure band engineering, externally controllable charge depletion, and crystallographic orientation. These attributes are combined to realize a prototype, mechanically based, exclusive-or logic element.

The domain at the nanometer scale presents new opportunities for realizing electro-mechanical transducers with ultralow power consumption, high sensitivity, integrated large-scale array architecture, and coupling to mesoscopic phenomena (1). As an advancement of microelectromechanical systems, which have become mainstream devices such as optical switches, ink jets, and accelerometers, nanoelectromechanical systems (NEMS) have shown great promise as highly sensitive detectors of mass (2, 3), displacement (4), charge (5), and energy (6). However, as electromechanical devices are scaled downward, transduction becomes increasingly difficult, hampering efforts to create finely controlled integrated systems. In spite of substantial progress in the field (7), an efficient, integrated, and customizable technique for actively driving and tuning NEMS resonators has remained elusive. Conventional approaches such as magnetomotive, electrostatic, and electrothermal techniques (7, 8) suffer from either low power efficiency, limited potential for integration, or poor nanoscale control over electromechanical coupling. In contrast, one of the earliest and most straightforward actuation methods, based on the piezoelectric effect, provides a means of directly converting an electric field into mechanical strain. Discovered by the Curie brothers in 1880 (9), it has since been widely applied in a multitude of systems ranging from clocks to microwave electromechanical filters and biosensors. However, new nanoscale functionality enabled by piezoelectric coupling has not yet been systematically explored with top-down NEMS devices.

We investigated the use of piezoelectric semiconductors as active structural materials for NEMS resonators. The active region of our nanomechanical devices consists of a 200-nm-thick epitaxially grown GaAs p-type/intrinsic/n-type (pin) diode (10). The clamped ends of the suspended structures lie on top of a sacrificial $\text{Al}_{0.8}\text{Ga}_{0.2}\text{As}$ layer, which is doped along with the substrate to allow the back side of the wafer to be used as a ground electrode. An n-doped layer serves as the top electrode, and finally, the charge-depleted high-resistance region in the middle forms the piezoelectrically active layer. Details on the pin junction doping profile and device

fabrication are presented in (11). We first focused on NEMS cantilevers, as depicted in Fig. 1A, which we used to gauge the efficiency of piezoelectric excitation. To ensure that the mechanical readout scheme was decoupled from charge-depletion effects, we employed optical interferometry (12) to sense motion so that unnecessary complications were not introduced into our analysis. During a typical measurement (Fig. 1B), an ac signal applied across the pin junction actuates the device at or near its resonance frequency, while the addition of dc voltage tunes the depletion-region width. Within the device, a transverse electric field, E_z , produces a longitudinal strain $\epsilon_j = d_{3j}E_z$, where d_{3j} is the anisotropic piezoelectric coefficient (13). A bending moment develops when the strain is asymmetrically distributed around the beam's neutral axis, which results in mechanical resonance under a suitable range of driving frequencies. The particular cantilever shown in Fig. 1 is found to have a resonance frequency of 8 MHz and a quality factor (Q) of 2700 (Fig. 1C). Our measurements are in agreement with the expected value for this structure's first out-of-plane vibrational mode. The piezoelectric effect is capable of driving the device with ac signals as low as 5 μV before the onset of thermomechanical fluctuations (Fig. 1C, inset), corresponding to approximately a single electronic charge on the cantilever itself. Assuming a maximum current flow of 1 nA at 5 μV of ac drive (14), the minimum required power consumption of this device approaches 5 fW, with ~ 1 nW being more representative of typical operating conditions (an ac drive of 10 mV) during actuation. Further improvement is expected from semiconductor band-structure optimization.

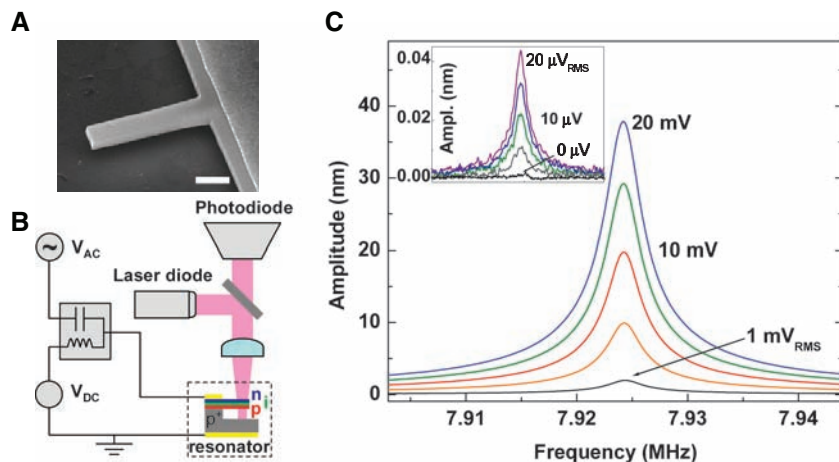


Fig. 1. Nanomechanical piezoelectric actuation. (A) GaAs cantilever with embedded pin diode structure. The dimensions are: length, 4 μm ; width, 0.8 μm ; and thickness, 0.2 μm . Scale bar, 1 μm . (B) Measurement setup. The bias T allows both dc and ac signals to be applied. All measurements were performed at room temperature and a pressure of 5 millitorr. (C) Frequency response around the resonance of a diode-embedded cantilever (pin-1) under 0 dc bias. Each line corresponds to a different-amplitude ac driving signal across the diode junction. (Inset) Response to drive signals of a few microvolts. (Each line, in order of increasing amplitude, corresponds to the addition of 5 μV .) The black line labeled "0 μV " corresponds to thermomechanical noise at a 10-Hz bandwidth and sets a lower limit on the ac driving signal that is required to generate an observable response. RMS, root mean squared.

¹Kavli Nanoscience Institute, California Institute of Technology, Pasadena, CA 91125, USA. ²IMEC, Kapeldreef 75, B-3001 Leuven, Belgium. ³Department of Physics, University of Alberta, and National Institute for Nanotechnology, Edmonton, Alberta, Canada.

*To whom correspondence should be addressed. E-mail: roukes@caltech.edu

These measurements demonstrate the efficiency of this integrated excitation technique, both in terms of charge and of power required. For comparison, magnetomotive and electrothermal NEMS actuation schemes are not easily realizable with comparable power efficiency, because their comparatively low impedance results in substantial current flow. Moreover, many alternative ac-

tuation schemes rely on external electromagnetic fields mediated by gates (electrostatic), solenoids (magnetomotive), or lasers (optothermal); hence, they are not readily incorporated into the active vibrating structure of a nanoscale device.

The strain generated by an electric field is concentrated within the highly resistive charge-depletion region. This allows us to adjust the

piezoelectric actuation efficiency by altering the depletion width with an applied voltage, in much the same way as capacitance is systematically altered in varactor diodes. This actuation effect, however, is unique to nanoscale semiconductor structures, where the characteristic device length scale (i.e., the thickness of the pin heterostructure) can become comparable to the depletion width. To verify this form of electromechanical coupling, we measured the performance of the cantilever under different dc bias conditions (Fig. 2A). As expected, the mechanical amplitude of the device's response strongly depends on the dc voltage. We developed a simple analytical model that combines two competing mechanisms that control actuation (11): (i) depletion-mediated strain (Fig. 2B and fig. S1) and (ii) variable resistance of the pin diode junction (fig. S2). Because strain is proportional to the voltage across the junction, lowering the resistance via excessive forward or reverse biasing of the diode leads to a reduction of actuation efficiency. However, this effect is not evident as long as the diode bias value lies below its "on" state and above breakdown, which are respectively determined to be at 0.7 and -3 V. To validate our predictions, we fabricated identical cantilevers from three pin diode junctions and measured their resonance amplitudes as a function of dc voltage. The diodes' doping profiles were designed to demonstrate three qualitatively different effects of depletion-mediated strain on actuation: (i) increasing resonance amplitude under decreasing voltage (pin-1), (ii) constant amplitude (pin-2), and (iii) decreasing amplitude (pin-3). We found good agreement between the observed and predicted mechanical response of these devices (Fig. 2C).

Another remarkable feature of NEMS fabricated from piezoelectric materials is voltage-induced resonance-frequency control. To demonstrate this, we patterned doubly clamped beams such as those shown in Fig. 3A. These structures are driven to resonance in the same fashion as are cantilevers. Shifts in resonance are clearly observed upon the dc-biasing of the device (Fig. 3B), because piezoelectric strain is converted into stress as a result of clamped-clamped boundary conditions (15). In the case of small perturbations, this behavior can be quantitatively described by the following expression (16)

$$\Delta f = -\sqrt{3Y/\rho} d_{3j}V/(2\pi t^2) \quad (1)$$

The elastic Young's modulus Y is 101 GPa, the density ρ is 5.3 g/cm^3 , t is the total device thickness (200 nm), Δf is the change in frequency, and V is the voltage. The above expression implies linear frequency-voltage dependence. In addition, because of the anisotropic nature of the piezoelectric coefficient, we expect to be able to control the slope of Δf by fabricating the beam along a prescribed direction. Both predictions are verified by the measurements displayed in Fig. 3C. The equal and opposite tuning slope of devices aligned along the [110] and $[-110]$ direc-

Fig. 2. Voltage-tunable depletion-mediated strain manifests itself as a change in actuation efficiency. **(A)** Frequency response of the same device as in Fig. 1, but with a fixed ac drive (10 mV) and a different dc bias. **(B)** Model electric-field distribution in a stereotypical pin junction. The colored lines correspond to the field under increasing applied voltage. The field lines are skewed toward the lower-doped side (in this case, the pink p-type layer), resulting in a different piezoelectric strain distribution that alters the actuation efficiency. **(C)** Normalized resonance amplitude versus dc bias voltage for three different pin diodes embedded in identically shaped cantilevers. For ease of comparison, the response of each device was normalized to its own amplitude at 0 dc volts. The ac driving signal was fixed at 10 mV. (Inset) Predicted behavior of the diodes (11).

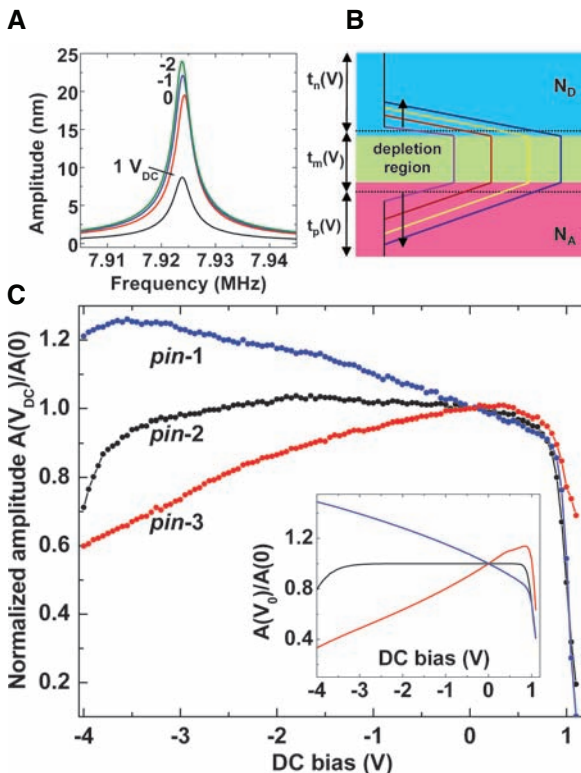
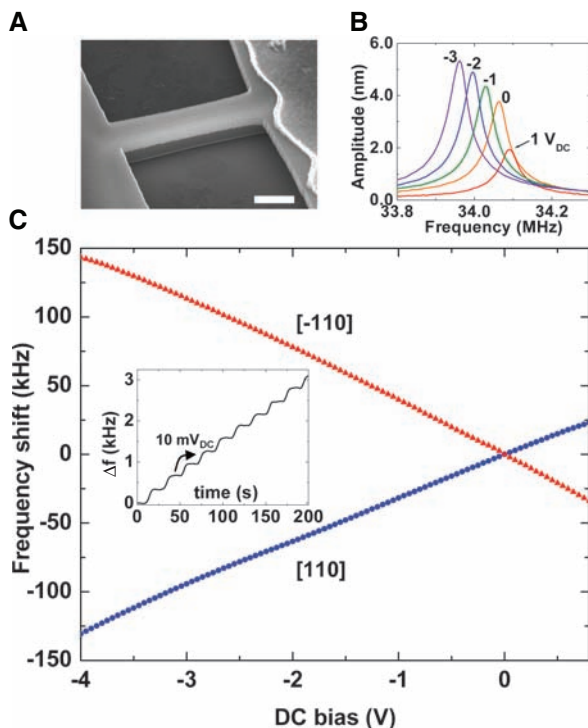


Fig. 3. Piezoelectric resonance-frequency control. **(A)** Doubly clamped beam structure with the same dimensions as in Fig. 1A. Scale bar, $1 \mu\text{m}$. **(B)** Frequency response near the beam's fundamental out-of-plane resonance mode. Each line corresponds to a different dc bias applied across the diode junction. The ac driving amplitude is fixed at 70 mV. **(C)** Phase-locked-loop measurements of resonance-frequency shift as a function of voltage. The blue and red lines correspond to beams fabricated along the [110] and $[-110]$ crystallographic directions, respectively. Their slopes have opposite signs because of piezoelectric anisotropy. (Inset) Time-dependent frequency shift under the stepwise addition of 10 mV. About 500 electronic charges were added to the beam at each step.



tions is characteristic of the opposite sign of d_{3j} along these directions. Fitting the slope of the steepest line to Eq. 1 yields a value of $d_{31} = -1.33$ pm/V, in excellent agreement with the accepted measured value along the [110] direction (13). Because stresses in cantilevers can relax by expanding or contracting, their frequency tunability is substantially lower than that of beams, as is evident by comparing Figs. 2A and 3B. The combination of integration, linearity, voltage efficiency, and crystallographic anisotropy of piezoelectric frequency tuning presents an advantage over other tuning mechanisms that rely on electrostatic force (5) or thermal stress (17). Devices that may benefit from the added functionality include parametric amplifiers (18), intrinsically cooled nanomechanical resonators (19), and voltage-controlled mechanical oscillators in frequency standards or sensing applications.

As a further example of the potential application of voltage-dependent frequency tuning, we demonstrated piezoelectric nanomechanical charge sensing. The inset of Fig. 3C shows the time progression of frequency during stepwise 10-mV increases in DC bias. Each step corresponds to the addition of ~ 2 kV/cm of field across the depletion region or ~ 500 electronic charges on the resonant device (20). The highest achievable resolution at room temperature is ~ 100 electrons, and it may be possible to approach single-electron resolution by using enhanced readout techniques, an optimized quality factor, and higher aspect-ratio beams (21). This suggests that, unlike other NEMS resonator sensors, which typically measure only mass accretion, tunable piezoelectric transducers could also serve as detectors of ionic species, making them attractive candidates for mass spectrometry applications (3).

Our ability to finely control the mechanical response of NEMS devices in a variety of ways

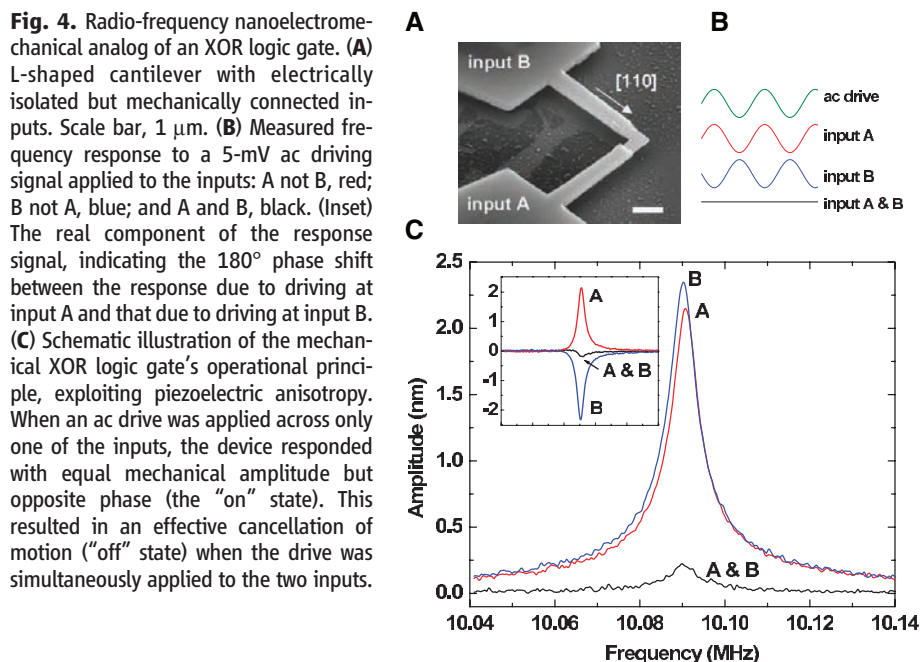
raises the intriguing possibility of creating elements for nanomechanical logic and computation. It is worth recalling that some of the earliest computers were mechanical, and interest in this concept has resurfaced with the advent of non-volatile carbon-nanotube memory elements (22). As an initial implementation of piezoelectric NEMS logic, we took advantage of the crystallographic anisotropy of d_{3j} . The prototype device (pictured in Fig. 4A) consists of an L-shaped cantilever with two separately addressable inputs for actuation. The top conducting portion of the structure was removed at the tip, resulting in a pair of mechanically bound but electrically isolated actuators. When driven from only input A or B, the entire structure resonates with a fundamental frequency of 10 MHz and a Q of 2000 (Fig. 4B). Because the two halves of the structure are aligned along crystallographically orthogonal directions, we observed that a stimulus at input A results in an equal-magnitude but opposite-phase mechanical response as the same stimulus applied at input B [Fig. 4, B (inset) and C] (23). Thus, when the a driving stimulus of the same magnitude was simultaneously applied to both inputs through a 0-degree power splitter, the response of the device was found to be substantially attenuated, as one would expect from a cancellation of motion. This device represents a prototype radio-frequency nanomechanical analog to an exclusive-or (XOR) logic gate with a demonstrated on/off ratio of 8:1. We envision the integration of NEMS logic in large-scale arrays that could carry out preliminary computations in the electromechanical domain before conventional digital processing (24). Potential advantages of this approach include lower net power consumption and greater functionality in computation.

We have demonstrated an approach to designing nanoelectromechanical systems from

piezoelectric semiconductors with tailored band structure, geometry, and crystallographic direction. The resulting electromechanical coupling phenomena, which rely entirely on intrinsic material properties, facilitate the creation of compact, tunable NEMS arrays for multidimensional sensing (25) and nanomechanical computing applications (24). The ability to regulate actuation efficiency through depletion-mediated strain in the semiconductor heterostructure's low-operating-power regime raises the prospect for developing efficient, high-speed electromechanical switches. Such devices may play an important role in selectively addressing individual elements in large-scale arrays of NEMS. Furthermore, the integration of a reliable and customizable frequency-tuning method adds a useful layer of functionality that has so far been absent in NEMS. Although not explored here, the reversibility of piezoelectric phenomena offers the potential for ultrasensitive electrical measurement of nanomechanical motion (26–29). Finally, all of the concepts presented here are transferrable to a wide variety of other materials beyond GaAs (such as AlN, SiC, or ZnO), which may provide enhanced electrical and mechanical properties.

References and Notes

- M. L. Roukes, *Phys. World* **14**, 25 (2001).
- J. Fritz *et al.*, *Science* **288**, 316 (2000).
- Y. T. Yang, C. Calegari, X. L. Feng, K. L. Ekinci, M. L. Roukes, *Nano Lett.* **6**, 583 (2006).
- M. D. LaHaye, O. Buu, B. Camarota, K. C. Schwab, *Science* **304**, 74 (2004).
- A. N. Cleland, M. L. Roukes, *Nature* **392**, 160 (1998).
- W. C. Fon, K. C. Schwab, J. M. Worlock, M. L. Roukes, *Nano Lett.* **5**, 1968 (2005).
- K. L. Ekinci, *Small* **1**, 786 (2005).
- I. Bargatin, I. Kozinsky, M. L. Roukes, *Appl. Phys. Lett.* **90**, 093116 (2007).
- P. Curie, J. Curie, *Bull. Soc. Minéral. Fr.* **3**, 90 (1880).
- Pin diode junctions were used because of their high electrical resistance, which is required for efficient actuation, and convenience in modeling voltage-dependent charge-depletion effects.
- Materials and methods are available as supporting material on *Science* Online.
- D. W. Carr, H. G. Craighead, *J. Vac. Sci. Technol.* **B15**, 2760 (1997).
- K. Fricke, *J. Appl. Phys.* **70**, 914 (1991).
- The actual measured current in the low-bias regime was typically between 0.001 and 1 μ A per 20 mV, which would lead to an even lower estimate of power consumption.
- B. Piekarski, D. Devoe, M. Dubey, R. Kaul, J. Conrad, *Sens. Actuat. A* **91**, 313 (2001).
- S. Timoshenko, D. H. Young, W. Weaver, *Vibration Problems in Engineering* (Wiley, New York, ed. 4, 1974).
- S. C. Jun *et al.*, *Nanotechnology* **17**, 1506 (2006).
- D. Rugar, P. Grütter, *Phys. Rev. Lett.* **67**, 699 (1991).
- C. H. Metzger, K. Karrai, *Nature* **432**, 1002 (2004).
- It is important to distinguish the total induced charge, which is dominated by the parasitic capacitance of the gold-wire-bond contact pads (and is much greater than 500 electronic charges per 10 mV of bias), from the charge on the NEMS device. The phase-locked-loop sampling rate was set to 10 Hz.
- One would ideally like to make devices as thin as possible to maximize charge sensitivity (see Eq. 1). However, surface-depletion effects in GaAs place practical constraints on this dimension.
- T. Rueckes *et al.*, *Science* **289**, 94 (2000).
- The small disparity between the response to a drive at input A and the response to input B is believed to be due



- to symmetry-breaking device inhomogeneities introduced during fabrication.
24. M. L. Roukes, *Electron Devices Meeting, 2004. IEDM Technical Digest. IEEE International* (Institute of Electrical and Electronics Engineers, Piscataway, NJ, 2004) pp. 539–542.
25. M. C. Lonergan *et al.*, *Chem. Mater.* **8**, 2298 (1996).
26. D. Devoe, *Sens. Actuat. A* **88**, 263 (2001).
27. R. G. Beck, M. A. Eriksson, R. M. Westervelt, K. L. Campman, A. C. Gossard, *Appl. Phys. Lett.* **68**, 3763 (1996).
28. Y. Zhang, M. P. Blencowe, *J. Appl. Phys.* **92**, 7550 (2002).
29. R. Knobel, A. N. Cleland, *Appl. Phys. Lett.* **81**, 2258 (2002).
30. This work was supported by the Defense Advanced Research Projects Agency Microsystems Technology Office Micro Gas Analyzer through Department of Interior contract no. NBCH1050001. We thank W. van de Graaf and S. Degroote for the epitaxial crystal deposition and P. Van Dorpe and J. M. Choi for discussions.

Supporting Online Material

www.sciencemag.org/cgi/content/full/317/5839/780/DC1
Materials and Methods
SOM Text
Figs. S1 and S2
References

8 May 2007; accepted 6 July 2007
10.1126/science.1144793

Label-Free, Single-Molecule Detection with Optical Microcavities

Andrea M. Armani,¹ Rajan P. Kulkarni,² Scott E. Fraser,^{1,2*} Richard C. Flagan,^{3*} Kerry J. Vahala¹

Current single-molecule detection techniques require labeling the target molecule. We report a highly specific and sensitive optical sensor based on an ultrahigh quality (Q) factor ($Q > 10^8$) whispering-gallery microcavity. The silica surface is functionalized to bind the target molecule; binding is detected by a resonant wavelength shift. Single-molecule detection is confirmed by observation of single-molecule binding events that shift the resonant frequency, as well as by the statistics for these shifts over many binding events. These shifts result from a thermo-optic mechanism. Additionally, label-free, single-molecule detection of interleukin-2 was demonstrated in serum. These experiments demonstrate a dynamic range of 10^{12} in concentration, establishing the microcavity as a sensitive and versatile detector.

Single-molecule fluorescence experiments have improved our understanding of many fundamental biological processes, such as protein folding kinetics (1), molecular transport (2, 3), and aspects of DNA replication (4). However, all of these breakthrough experiments required labeling of the target molecule (5, 6). In the case of surface-enhanced Raman spectroscopy (SERS), total internal reflection fluorescence microscopy (TIRF) and confocal microscopy, this label behaves as an amplifier for an otherwise undetectable single-molecule signal; however, it also restricts an experiment's scope, because there must be prior knowledge of the target's presence and the target molecule must be modified to incorporate the label (7–12). There have been several attempts to overcome this need to label the analyte by developing label-free sensing technologies, ranging from fiber-optic waveguides (13) and nanowires (14) to nanoparticle probes (15), biochips (16), and mechanical cantilevers (17), but none has achieved single-molecule sensitivity.

Optical microcavities have been proposed as a powerful method to achieve label-free detection of single molecules because the resonant recirculation of light within a microcavity allows the light to sample target molecules many more times (18–21). For example, in a simple optical wave-

guide sensor, the input light has only one opportunity to interact with the target molecule. In contrast, by using a planar microcavity with a quality (Q) factor of 10^8 (Fig. 1A), the molecule is sampled more than 100,000 times. This increased sampling manifests itself both as a shift of the resonant wavelength and as a decrease in the Q factor as the target molecules directly change the optical path length and/or the cavity loss of the sensor (18, 19). The current work extends these ideas by adding a new mechanism through which molecules can induce a resonant wavelength shift. In particular, it will be shown that a thermo-optic mechanism greatly enhances detection sensitivity. Biochemically functionalizing the surface of the resonator to recognize the target molecule should provide an excellent platform for ultrasensitive

detection and specific identification of dissolved, unlabeled target molecules (22, 23).

We fabricated planar arrays of silica microtoroid whispering-gallery resonators (Fig. 1A) using a simple three-step process: (i) circular oxide pads were lithographically defined; (ii) the silicon wafer was selectively etched with xenon difluoride, forming arrays of silica microdisks; and (iii) the microdisks were reflowed with a CO_2 laser (24, 25). Microtoroids offer Q factors in excess of 100 million for enhanced detection sensitivity, and their silica surfaces are readily functionalized for specific detection of biomolecules (23). The microtoroids were coupled to a tunable laser and detector by a tapered optical fiber waveguide and were immersed in water within a microaquarium with syringe inlets for introducing samples (26). The tapered optical fiber waveguide launches light into the whispering-gallery mode at the periphery of the microtoroid. The resonant whispering-gallery mode is partially confined inside the silica microtoroid, but it evanesces into the liquid environment (Fig. 1B). Thus, the light interacts strongly with the molecules once they are captured on the toroidal surface, in a manner similar to the way that a surface plasmon resonance (SPR) sensor interrogates a sample (27). The silica surfaces were sensitized either with biotin or antibodies to capture specific molecules [avidin or the target antigen, respectively (26)]. This binding interaction creates red shifts of the resonant wavelength that can be monitored in real time (26). In the static condition without the presence of biological molecules, the opposing thermo-optic

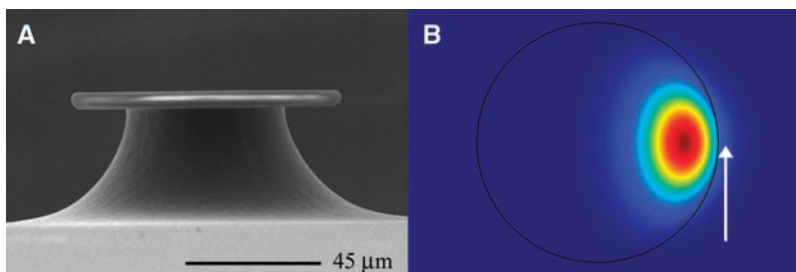


Fig. 1. The microtoroid resonator biological sensor. **(A)** A scanning electron micrograph (SEM) image of the UHQ microtoroid optical resonator. The silica microtoroid is fabricated on a silicon wafer using planar lithography and reflowed using a CO_2 laser. The typical microtoroid diameter used in this work was 80 μm . **(B)** A finite element model [FEMLAB (COMSOL, Burlington, Massachusetts, USA)] of a 4- μm minor diameter microtoroid resonator immersed in water. Although the majority of the optical field resides in the silica toroid, a portion of the field evanesces into the environment (indicated by a white arrow). The interaction of the whispering-gallery mode with the environment, specifically molecules bound on the surface of the toroid, enables the ultrasensitive detection.

¹Department of Applied Physics, MC 128-95, California Institute of Technology, Pasadena, CA 91125, USA. ²Division of Biology, MC 139-74, California Institute of Technology, Pasadena, CA 91125, USA. ³Division of Chemistry and Chemical Engineering, MC 210-41, California Institute of Technology, Pasadena, CA 91125, USA.

*To whom correspondence should be addressed. E-mail: sefraser@caltech.edu (S.E.F.); flagan@caltech.edu (R.C.F.)